Macromolecules

pubs.acs.org/Macromolecules Article

# Functional Nano-Objects Prepared via Living Anionic Polymerization-Induced Self-Assembly (LAPISA) of Polar Vinyl Monomers

Di Li and Guowei Wang*

Cite This: Macromolecules 2025, 58, 8898−8908 Read Online

ACCESS | Metrics & More | Article Recommendations | Supporting Information

**ABSTRACT:** The living anionic polymerization-induced self-assembly (LAPISA) process, possessing the common merits of both LAP and PISA techniques, facilitated and promoted research on self-assembly. However, the limited monomers available for the LAPISA process significantly restricted the preparation and application of the corresponding nano-objects. Herein, polar monomers were appended to the LAPISA system, and functional nano-objects were targeted. By optimizing 1,1-diphenylhexane lithium ($DPH^-Li^+$) and potassium bis(trimethylsilyl) amide (KHMDS) as a co-initiation system and *tri*-isobutylaluminum ($iBu_3Al$) as an additive, the sequential LAP of *tert*-butyl methacrylate (*t*BMA) and LAPISA of 4-vinylpyridine (4VP) were successfully realized at room temperature of 25 °C. By adjusting $[KHMDS]_0/[DPH^-Li^+]_0$, $[iBu_3Al]_0/[4VP]_0$, targeted $M_{n,P4VP}/M_{n,PtBMA}$, and toluene content in toluene/tetrahydrofuran (wt $\%_{Tol}$), nano-objects with different morphologies, including spheres, worms, and vesicles, were prepared. The P*t*BMA-*b*-P4VP diblock copolymer and nano-objects were prepared in a controlled manner. The crosslinking reaction between the pyridine groups on P4VP and 1,4-dibromobutane was performed via the quaternization reaction, which enabled the stabilization of the nano-objects. Using the functional pyridine groups in the core region, silver ions ($Ag^+$) and metal ($Ag^0$) were introduced into the nano-objects by sequential complexation and reduction reactions, and the $Ag^0$ content could be well controlled by modulating the $[Ag^+]_0/[4VP]_0$. The successful LAPISA of polar monomers provided an efficient and alternate route to functional nano-objects and organic/inorganic nanocomposites.

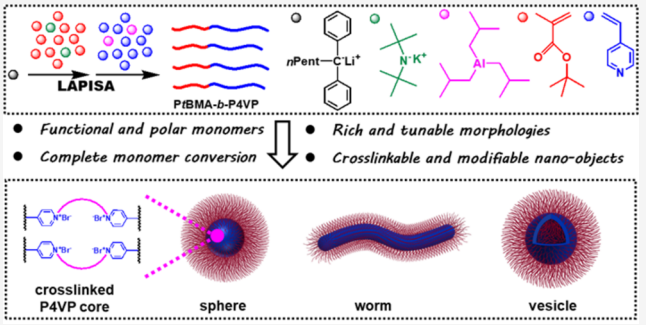




## INTRODUCTION

Block copolymer nano-objects have attracted widespread attention in the past few decades due to their diverse morphologies,[1−5] which have been widely used in nanocomposite materials,[6−8] catalytic materials,[9−11] optoelectronic materials,[12−14] biomedicines,[15,16] batteries,[17,18] and so on. Block copolymer nano-objects are typically prepared by traditional self-assembly, which disperses the purified block copolymer in a selective solvent and uses the difference in solubility of each block to achieve nano-objects with various morphologies, such as spheres, worms, and vesicles.[2,19,20] However, the low solid content (<1 wt %) and multistep nature of this method severely restrict the industrial application of block copolymer nano-objects.[21−23]

Polymerization-induced self-assembly (PISA) is a process that realizes the polymerization and self-assembly of block copolymers in the same system. As monomers polymerize, the degree of polymerization (DP) of the second block gradually increases, and the solubility of the copolymer decreases, driving the *in situ* self-assembly of the block copolymer.[24] The most significant advantage of PISA is its ability to polymerize and assemble at high solid content (up to 50 wt %) with simple operations,[24,25] making it the most valuable technology for the industrial production of block copolymer nano-objects. The emergence of various "living"/controlled radical polymerizations (CRP), such as atom transfer radical polymerization (ATRP),[26−29] reversible addition−fragmentation chain transfer polymerization (RAFT),[30,31] and nitroxide-mediated polymerization (NMP),[32,33] has provided an opportunity for the rapid development of PISA technology. Efforts have also been made to introduce other polymerization techniques such as tellurium-mediated living radical polymerization (TERP)[34] and ring-opening metathesis polymerization (ROMP)[35,36] into the PISA process. Among all these polymerization mechanisms, the RAFT is mostly combined with the PISA technique, targeting the functional block copolymer nano-objects.[37−42]

Received: May 31, 2025
Revised: July 24, 2025
Accepted: July 31, 2025
Published: August 11, 2025





https://doi.org/10.1021/acs.macromol.5c01443
Macromolecules 2025, 58, 8898−8908

Scheme 1. Illustration of the LAPISA Process of Polar Vinyl Monomers and Stabilization of the Formed Nano-Objects

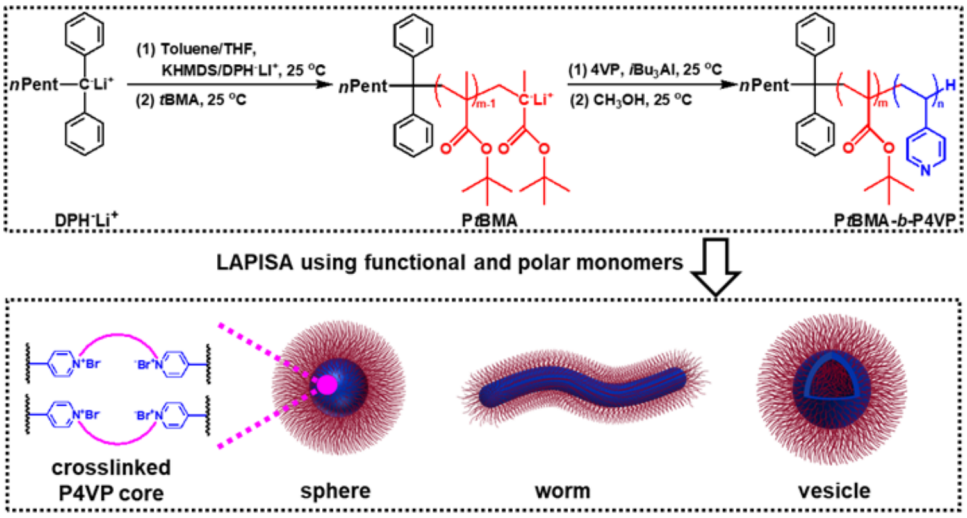


Living anionic polymerization (LAP), as the oldest living polymerization process, is still the most powerful tool for the synthesis of model copolymers with specific structures, molecular weights (MWs), and narrow molecular weight distributions (MWDs) due to the absence of spontaneous termination and transfer of active species under appropriate conditions.[43−46] In 2007, Wang and co-workers synthesized polybutadiene-*b*-polystyrene (PB-*b*-PS) diblock copolymers by the LAP process in *n*-hexane, achieving the commercial-scale synthesis of nano-objects with diverse morphologies, including spheres, flowers, Janus, and worms.[47] These nano-objects were further stabilized with a divinylbenzene (DVB) agent, providing initial evidence for the potential application of LAP to PISA. Later, based on the polyisoprene-*b*-polystyrene (PI-*b*-PS) diblock copolymer, our group systematically explored the influence of factors, such as the MWs of the stabilizer block, targeted $M_{n,PS}/M_{n,PI}$, and solid content, on the morphological evolution of nano-objects in *n*-heptane.[48,49] By introducing a solvophobic homopolymer and performing a cooperative self-assembly process, we successfully fabricated higher-order morphologies like sponges, further expanding the application of LAP in PISA.[50] Especially, the LAP mechanism featured complete monomer conversion, absence of contaminants from catalysts, and excellent controllability. However, the monomers available for the preparation of nano-objects via living anionic polymerization-induced self-assembly (LAPISA) are typical dienes, styrene and its derivatives, which have fewer groups and limited functions. The LAP of polar vinyl monomers, such as (meth)acrylates and vinylpyridine, is prone to side reactions, which limits the application of LAPISA in the field of functional nano-objects. Thus, the LAPISA process of polar vinyl monomer is still challenged and, meanwhile, has much importance.

In this work, polar vinyl monomers are introduced into the LAPISA process for the first time (Scheme 1). First, using the mixture of 1,1-diphenylhexane lithium ($DPH^-Li^+$) and potassium bis(trimethylsilyl)amide (KHMDS) as the co-initiation system, *tri*-isobutylaluminum ($iBu_3Al$) as an additive, toluene and/or tetrahydrofuran (THF) as solvents, *tert*-butyl methacrylate (*t*BMA) as the first monomer, and 4-vinylpyridine (4VP) as the second monomer, the LAPISA was performed to prepare P*t*BMA-*b*-P4VP nano-objects under room temperature of 25 °C. The effects of $[KHMDS]_0/[DPH^-Li^+]_0$, $[iBu_3Al]_0/[4VP]_0$, targeted $M_{n,P4VP}/M_{n,PtBMA}$, and toluene content (wt $\%_{Tol}$) on the LAPISA process were systematically investigated. Subsequently, using the quaternization reaction on the 4VP units, the P4VP core was crosslinked, and the nano-objects were stabilized. Finally, $Ag^0$ was introduced into the P4VP core via the first coordination of $Ag^+$ and the second reduction reaction. The polymers were characterized by size exclusion chromatography (SEC) and proton nuclear magnetic resonance ($^1H$ NMR) spectroscopy. The morphologies of the nano-objects were monitored by transmission electron microscopy (TEM), scanning electron microscopy (SEM) and dynamic light scattering (DLS). The nanocomposites were analyzed by ultraviolet−visible spectroscopy (UV−vis) and thermogravimetric analysis (TGA).

## RESULTS AND DISCUSSION

**Controllability of LAPISA for P*t*BMA-*b*-P4VP Nano-Objects.** For P*t*BMA-*b*-P4VP nano-objects, the LAP of *t*BMA was first performed by employing KHMDS and/or $DPH^-Li^+$ as the initiator, and THF as the solvent. As shown in Table S1, when single KHMDS was used as the initiator at room temperature (25 °C), the experimental $M_{n,PtBMA}$ evaluated by the SEC measurement (109 800 g/mol) was significantly higher than the theoretical $M_{n,PtBMA}$ (10 000 g/mol). Meanwhile, $M_w/M_n$ reached 1.33, indicating an uncontrollable LAP process (Figure S1). This could be attributed to the relatively lower initiation efficiency of KHMDS for the *t*BMA monomer. When a single $DPH^-Li^+$ was used as the initiator, the $M_w/M_n$ of P*t*BMA decreased to 1.28, which was still larger than the value expected by a typical LAP process (Figure S2). Alternatively, when KHMDS and $DPH^-Li^+$ were synergistically introduced, polymerization could be well controlled. Keeping the $[KHMDS]_0/[DPH^-Li^+]_0$ ratios in the range of 0.05 to 1.0, $M_w/M_n$ values below 1.15 could be readily realized. Additionally, from the typical $^1H$ NMR spectrum for crude $PtBMA_{37}$ (Figure S3), the absence of resonance signals (around 5.46 and 6.00 ppm) for the protons ($CH_2$=C−) on double bonds confirmed the complete conversion of the *t*BMA monomer. Obviously, in the first polymerization stage, the bimetallic co-initiation system contributed to excellent control of the LAP on the *t*BMA monomer. According to the


https://doi.org/10.1021/acs.macromol.5c01443
Macromolecules 2025, 58, 8898−8908

Table 1. Formulation and Characterization Data for the P*t*BMA-*b*-P4VP Diblock Copolymer with Different $[i\text{Bu}_3\text{Al}]_0/[4\text{VP}]_0$ Ratios and Targeted $M_{n,\text{P4VP}}/M_{n,\text{PtBMA}}$ Using THF as a Solvent[b]

| sample | $[i\text{Bu}_3\text{Al}]_0/[4\text{VP}]_0$ | targeted $M_{n,\text{P4VP}}/M_{n,\text{PtBMA}}$ | $M_{n,\text{PtBMA}}$/g/mol[a] | $M_w/M_n$[a] | $M_{n,\text{PtBMA-}b\text{-P4VP}}$/g/mol[a] | $M_w/M_n$[a] | morphologies[c] | DLS[d] Z-average | DLS[d] PDI |
|---|---|---|---|---|---|---|---|---|---|
| $\text{PtBMA}_{37}$-*b*-$\text{P4VP}_{309}$ | 0 | 6.0 | 5200 | 1.13 | 37,700 | 1.50 | sphere and short worm | 44 | 0.06 |
| $\text{PtBMA}_{32}$-*b*-$\text{P4VP}_{300}$ | 0.005 | 6.0 | 4600 | 1.10 | 36,100 | 1.44 | sphere | 145 | 0.16 |
| $\text{PtBMA}_{35}$-*b*-$\text{P4VP}_{250}$ | 0.01 | 6.0 | 5000 | 1.08 | 31,300 | 1.19 | long worm | 210 | 0.03 |
| $\text{PtBMA}_{34}$-*b*-$\text{P4VP}_{264}$ | 0.02 | 6.0 | 4800 | 1.13 | 32,600 | 1.21 | long worm | 418 | 0.01 |
| $\text{PtBMA}_{35}$-*b*-$\text{P4VP}_{322}$ | 0 | 12.0 | 4900 | 1.11 | 38,800 | 2.21 | short worm and vesicle | 1954 | 0.12 |
| $\text{PtBMA}_{34}$-*b*-$\text{P4VP}_{655}$ | 0.005 | 12.0 | 4800 | 1.16 | 73,700 | 1.45 | sphere | 154 | 0.07 |
| $\text{PtBMA}_{28}$-*b*-$\text{P4VP}_{522}$ | 0.01 | 12.0 | 4000 | 1.08 | 58,900 | 1.25 | vesicle | 4531 | 0.26 |
| $\text{PtBMA}_{30}$-*b*-$\text{P4VP}_{501}$ | 0.02 | 12.0 | 4300 | 1.10 | 57,000 | 1.22 | vesicle | 344 | 0.34 |

[a] $M_n$ and $M_w/M_n$ were obtained by SEC measurements using DMF containing 1.4 g/L LiBr as the eluent and PMMA as the standard. [b] $\text{DP}_{\text{PtBMA}} = M_{n,\text{PtBMA}}/142.2$ and $\text{DP}_{\text{P4VP}} = (M_{n,\text{PtBMA-}b\text{-P4VP}} - M_{n,\text{PtBMA}})/105.1$, where 142.2 and 105.1 are the MWs of *t*BMA and 4VP monomers, respectively. [c] Morphologies were monitored by TEM. [d] The Z-average size and polydispersity index (PDI) were determined by DLS measurement.

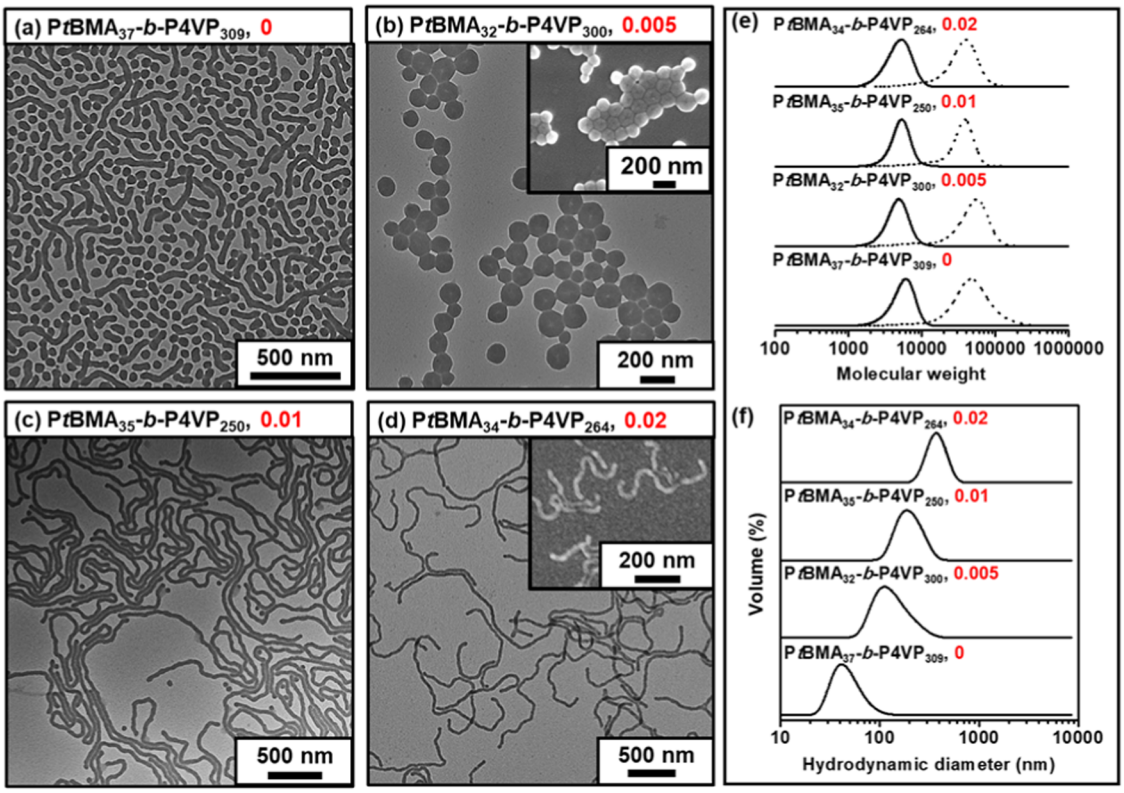


**Figure 1.** TEM and SEM images of nano-objects generated with varied $[i\text{Bu}_3\text{Al}]_0/[4\text{VP}]_0$ ratios: (a) 0, (b) 0.005, (c) 0.01, and (d) 0.02, respectively, while designing the targeted $M_{n,\text{PtBMA}}$ around 4000−5500, targeted $M_{n,\text{P4VP}}/M_{n,\text{PtBMA}}$ as 6.0, solid content of 15 wt %, and THF as the solvent. Samples were diluted to 0.1−0.3 wt % dispersions in THF, and samples on the copper grid were not stained. (e) SEC traces for the macroinitiator P*t*BMA and the corresponding P*t*BMA-*b*-P4VP diblock copolymers obtained in the LAPISA process with varied $[i\text{Bu}_3\text{Al}]_0/[4\text{VP}]_0$ ratios. DMF containing LiBr (1.4 g/L) was used as the eluent, and PMMA was used as the standard. (f) DLS results for the corresponding nano-objects in THF.

literature,[51] this could be attributed to the partial replacement of $Li^+$ by $K^+$ counterions at the chain ends upon the addition of KHMDS. Correspondingly, bulk bis(trimethylsilyl)amide tended to accumulate around the chain ends, leading to a reduced polymerization rate of the LAP of *t*BMA. To avoid the use of excess additive, in the following experiment, a $[\text{KHMDS}]_0/[\text{DPH}^-\text{Li}^+]_0$ of 1.0 was adopted in all cases.

Preliminarily, the above comparison on LAP using the KHMDS/$\text{DPH}^-\text{Li}^+$ combination, a single KHMDS or $\text{DPH}^-\text{Li}^+$indicated that KHMDS has low initiation efficiency, and $\text{DPH}^-\text{Li}^+$ acted as the dominant initiator in the LAPISA process. To verify this conclusion, low-molecular-weight P*t*BMAs were further synthesized using $\text{DPH}^-\text{Li}^+$or KHMDS/$\text{DPH}^-\text{Li}^+$ ($[\text{KHMDS}]_0/[\text{DPH}^-\text{Li}^+]_0$ of 1.0) as initiators and employed as models for MALDI-TOF MS characterization. As shown in Figure S4, the MALDI-TOF MS spectra for PtBMA initiated by both $\text{DPH}^-\text{Li}^+$ and KHMDS/$\text{DPH}^-\text{Li}^+$ displayed a series of peaks, which were separated by the mass of a *t*BAM unit (142.2 Da). For P*t*BMA initiated by $\text{DPH}^-\text{Li}^+$, one series of peaks ($n \times 142.2 + 23.0 + 238.2$) was


https://doi.org/10.1021/acs.macromol.5c01443
Macromolecules 2025, 58, 8898−8908

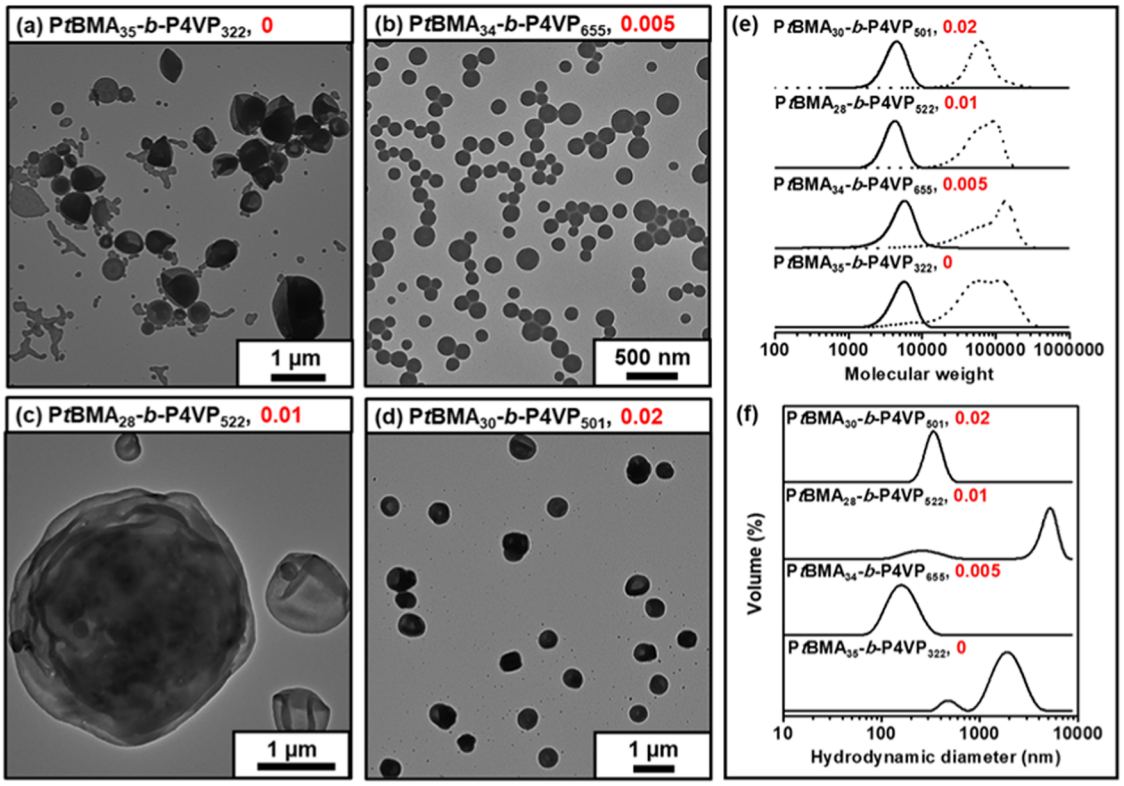


**Figure 2.** TEM and SEM images of nano-objects generated with varied $[i\mathrm{Bu_3Al}]_0/[4\mathrm{VP}]_0$ ratios: (a) 0, (b) 0.005, (c) 0.01, and (d) 0.02, respectively, while designing the targeted $M_{n,\mathrm{PtBMA}}$ around 4000−5500, targeted $M_{n,\mathrm{P4VP}}/M_{n,\mathrm{PtBMA}}$ as 12.0, solid content as 15 wt %, and THF as the solvent. Samples were diluted to 0.1−0.3 wt % dispersions in THF, and samples on the copper grid were not stained. (e) SEC traces for the macroinitiator P*t*BMA and the corresponding P*t*BMA-*b*-P4VP diblock copolymers obtained in the LAPISA process with varied $[i\mathrm{Bu_3Al}]_0/[4\mathrm{VP}]_0$. DMF containing LiBr (1.4 g/L) was used as the eluent, and PMMA was used as the standard. (f) DLS results for the corresponding nano-objects in THF.

observed. For P*t*BMA initiated by KHMDS/DPH$^-$Li$^+$, two series of peaks ($n \times 142.2 + 23.0 + 238.2$ and $n \times 142.2 + 39.0 + 238.2$) could be discriminated, which were attributed to P*t*BMA incorporated with $Na^+$ or $K^+$ ions, respectively. Thus, with the analysis of the data in Table S1 and the MALDI-TOF MS results, it could be deduced that LAP was dominantly initiated by DPH$^-$Li$^+$ rather than KHMDS, and the latter was just used as an additive to improve the controllability of the polymerization.

Subsequently, in the second polymerization stage, the 4VP monomer was added and polymerized. With an increase of 4VP monomer conversion, the P*t*BMA block was extended with a P4VP block, and the P*t*BMA-*b*-P4VP diblock copolymer was generated. Typically, THF is a good solvent for P*t*BMA but a poor solvent for P4VP. Thus, unlike the homogeneous polymerization of the *t*BMA monomer in the first polymerization stage, the poor solubility of the P4VP block in THF resulted in a heterogeneous LAPISA process in the second polymerization stage. Additionally, in the second polymerization stage, the unavoidable side reaction on 4VP would significantly affect the polymerization. Referring to the literature,[52] $i\mathrm{Bu_3Al}$ was added to address this problem, as $i\mathrm{Bu_3Al}$ could be used to efficiently stabilize living species. To evaluate the controllability of the LAPISA process, the effect of $i\mathrm{Bu_3Al}$ on the LAPISA process was carefully studied in the following section.

As shown in Table 1, a series of LAPISA formulations with varied $[i\mathrm{Bu_3Al}]_0/[4\mathrm{VP}]_0$ ratios were prepared at room temperature of 25 °C, while designing the targeted $M_{n,\mathrm{PtBMA}}$ around 4000−5500, targeted $M_{n,\mathrm{P4VP}}/M_{n,\mathrm{PtBMA}}$ as 6.0, and solid content as 15 wt %. In the absence of $i\mathrm{Bu_3Al}$ ($[i\mathrm{Bu_3Al}]_0/[4\mathrm{VP}]_0 = 0$), a P*t*BMA$_{37}$-*b*-P4VP$_{309}$ diblock copolymer with an $M_w/M_n$ of 1.50 was prepared, indicating an uncontrollable LAPISA process. Nevertheless, a mixture of spherical and short worm-like nano-objects was collected by TEM (Figure 1a). When $[i\mathrm{Bu_3Al}]_0/[4\mathrm{VP}]_0$ was increased to 0.005, a P*t*BMA$_{32}$-*b*-P4VP$_{300}$ diblock copolymer with an $M_w/M_n$ of 1.44 was generated. The TEM and SEM images cooperatively confirmed that vesicles with a relatively thick wall were formed (Figure 1b). When $[i\mathrm{Bu_3Al}]_0/[4\mathrm{VP}]_0$ was further increased to 0.01 and 0.02, P*t*BMA$_{35}$-*b*-P4VP$_{250}$ and P*t*BMA$_{34}$-*b*-P4VP$_{264}$ diblock copolymers with relatively lower $M_w/M_n$ of around 1.20, respectively, were obtained. The LAPISA was well controlled in these two cases, and the long worm-like nano-objects could be clearly distinguished by TEM and SEM images (Figure 1c,d). Meanwhile, the DLS measurement results were consistent with those derived from the TEM and SEM images (Figure 1f). According to the SEC curves, it could be found that the $M_w/M_n$ of P*t*BMA was always below 1.13. However, after the polymerization of the 4VP monomer, the $M_w/M_n$ was broadened in the cases with a lowered $[i\mathrm{Bu_3Al}]_0/[4\mathrm{VP}]_0$ (Figure 1e). Uniquely, diblock copolymers with similar $M_{n,\mathrm{P4VP}}/M_{n,\mathrm{PtBMA}}$, but different $M_w/M_n$ contributed to the formation of nano-objects with different morphologies.

Alternatively, by controlling the targeted $M_{n,\mathrm{PtBMA}}$ around 4000−5500, targeted $M_{n,\mathrm{P4VP}}/M_{n,\mathrm{PtBMA}}$ as 12.0, and solid content as 15 wt %, LAPISA was also performed while varying the molar ratio $[i\mathrm{Bu_3Al}]_0/[4\mathrm{VP}]_0$. The P*t*BMA$_{35}$-*b*-P4VP$_{322}$


https://doi.org/10.1021/acs.macromol.5c01443
Macromolecules 2025, 58, 8898−8908

Table 2. Formulation and Characterization Data for the P*t*BMA-*b*-P4VP Diblock Copolymer with Different Targeted $M_{n,P4VP}/M_{n,PtBMA}$ ratios, and Weight Content of Toluene in the Toluene/THF Solvent (wt $\%_{Tol}$).

| | | | | | | | | | DLS[d] | |
|---|---|---|---|---|---|---|---|---|---|---|
| sample | wt $\%_{Tol}$ | targeted $M_{n,P4VP}/M_{n,PtBMA}$ | $M_{n,PtBMA}$/g/mol[a] | $M_w/M_n$[a] | $M_{n,PtBMA\text{-}b\text{-}P4VP}$/g/mol[a] | $M_w/M_n$[a] | $DP_{P4VP}$[b] | morphology[c] | Z-average | PDI |
| $PtBMA_{34}$-*b*-$P4VP_{107}$ | 0 | 3.0 | 4800 | 1.17 | 16,100 | 1.14 | 107 | irregular morphology | 4 | 0.03 |
| $PtBMA_{35}$-*b*-$P4VP_{195}$ | 0 | 4.0 | 5000 | 1.16 | 25,500 | 1.16 | 195 | short worm | 49 | 0.17 |
| $PtBMA_{34}$-*b*-$P4VP_{264}$ | 0 | 6.0 | 4800 | 1.13 | 32,600 | 1.21 | 264 | long worm | 418 | 0.01 |
| $PtBMA_{31}$-*b*-$P4VP_{318}$ | 0 | 9.0 | 4400 | 1.13 | 37,800 | 1.19 | 318 | worm and vesicle | 382 | 0.16 |
| $PtBMA_{30}$-*b*-$P4VP_{501}$ | 0 | 12.0 | 4300 | 1.10 | 57,000 | 1.22 | 501 | vesicle | 344 | 0.34 |
| $PtBMA_{34}$-*b*-$P4VP_{580}$ | 0 | 15.0 | 4900 | 1.13 | 65,900 | 1.32 | 580 | precipitate | | |
| $PtBMA_{34}$- *b*-$P4VP_{138}$ | 25 | 3.0 | 4800 | 1.15 | 19,300 | 1.14 | 138 | sphere | 41 | 0.01 |
| $PtBMA_{33}$-*b*-$P4VP_{237}$ | 25 | 6.0 | 4700 | 1.18 | 29,600 | 1.13 | 237 | sphere and worm | 99 | 0.04 |
| $PtBMA_{31}$-*b*-$P4VP_{358}$ | 25 | 9.0 | 4400 | 1.13 | 42,000 | 1.16 | 358 | vesicle | 142 | 0.04 |
| $PtBMA_{37}$-*b*-$P4VP_{606}$ | 25 | 12.0 | 5200 | 1.17 | 68,900 | 1.23 | 606 | vesicle | 113 | 0.04 |
| $PtBMA_{34}$- *b*-$P4VP_{49}$ | 50 | 1.0 | 4900 | 1.12 | 10,000 | 1.21 | 49 | sphere | 36 | 0.10 |
| $PtBMA_{37}$- *b*-$P4VP_{70}$ | 50 | 2.0 | 5300 | 1.16 | 12,700 | 1.17 | 70 | sphere | 46 | 0.11 |
| $PtBMA_{34}$- *b*-$P4VP_{126}$ | 50 | 3.0 | 4800 | 1.13 | 18,000 | 1.14 | 126 | sphere | 65 | 0.24 |
| $PtBMA_{33}$- *b*-$P4VP_{218}$ | 50 | 4.0 | 4700 | 1.15 | 27,600 | 1.14 | 218 | sphere and short worm | 44 | 0.18 |
| $PtBMA_{35}$- *b*-$P4VP_{253}$ | 50 | 6.0 | 5000 | 1.09 | 31,600 | 1.16 | 253 | short worm | 290 | 0.46 |
| $PtBMA_{33}$- *b*-$P4VP_{302}$ | 50 | 8.0 | 4700 | 1.18 | 36,400 | 1.15 | 302 | precipitate | | |
| $PtBMA_{30}$- *b*-$P4VP_{45}$ | 75 | 1.0 | 4300 | 1.11 | 9,600 | 1.27 | 45 | sphere | 29 | 0.01 |
| *b*-$P4VP_{30}$- *b*-$P4VP_{87}$ | 75 | 2.0 | 4300 | 1.09 | 13,400 | 1.19 | 87 | short worm | 164 | 0.15 |
| $PtBMA_{35}$- *b*-$P4VP_{50}$ | 100 | 1.0 | 5000 | 1.14 | 10,300 | 1.25 | 50 | short worm | 110 | 0.42 |

[a]$M_n$ and $M_w/M_n$ were obtained by SEC measurements using DMF containing 1.4 g/L LiBr as the eluent and PMMA as the standard. [b]$DP_{PtBMA} = M_{n,PtBMA}/142.2$ and $DP_{P4VP} = (M_{n,\ PtBMA\text{-}b\text{-}P4VP} - M_{n,\ PtBMA})/105.1$, where 142.2 and 105.1 are the MWs of *t*BMA and 4VP monomers, respectively. [c]Morphologies were monitored by TEM. [d]The Z-average size and polydispersity index (PDI) were determined by DLS measurement.

diblock copolymer with an $M_w/M_n$ of 2.21 was prepared in the absence of $i$Bu$_3$Al ($[i\text{Bu}_3\text{Al}]_0/[4\text{VP}]_0 = 0$) (Figure 2e), indicating an uncontrolled LAPISA process. For $[i\text{Bu}_3\text{Al}]_0/[4\text{VP}]_0 = 0.005$, the $M_w/M_n$ of the generated $PtBMA_{34}$-*b*-$P4VP_{655}$ diblock copolymer decreased to 1.45, which was still out of control. For $[i\text{Bu}_3\text{Al}]_0/[4\text{VP}]_0$ of 0.01, $PtBMA_{28}$-*b*-$P4VP_{522}$ with an $M_w/M_n$ of 1.25 and a shoulder peak was observed. Furthermore, $PtBMA_{30}$-*b*-$P4VP_{501}$ diblock copolymer with an $M_w/M_n$ of 1.22 and a monomodal peak were generated for $[i\text{Bu}_3\text{Al}]_0/[4\text{VP}]_0$ of 0.02. Again, it could be discriminated that the control of the LAPISA was improved with the increase of $[i\text{Bu}_3\text{Al}]_0/[4\text{VP}]_0$. Correspondingly, only the $PtBMA_{30}$-*b*-$P4VP_{501}$ diblock copolymer formed uniform vesicles with thick walls (Figure 2d). However, $PtBMA_{28}$-*b*-$P4VP_{522}$, $PtBMA_{34}$-*b*-$P4VP_{655}$, and $PtBMA_{35}$-*b*-$P4VP_{322}$ diblock copolymers contributed to the formation of a mixture of spheres or vesicles with uneven sizes (Figure 2a–c). Similarly, the DLS results revealed a consistent size tendency as those from the TEM measurement (Figure 2f). Thus, all of the TEM, SEM, SEC, and DLS results indicated that the presence of $i$Bu$_3$Al was essential for a controlled LAPISA process, especially for systems with relatively higher $M_{n,P4VP}/M_{n,PtBMA}$.

Based on the above results, as well as a report in the literature,[52,53] the function of $i$Bu$_3$Al can be explained as follows. That is, the electron-deficient Al atom in $i$Bu$_3$Al tends to coordinate with the N atom on the pyridine ring, transferring electron density from the double bonds of 4VP to Al atom. The reduced electron density enhances the attack of the 4VP monomer by the living P*t*BMA species, increasing cross-propagation while suppressing self-propagation, thereby ensuring complete initiation from the P*t*BMA species. Additionally, the coordination between $i$Bu$_3$Al and the N atom reduces the likelihood of the capture of living species by the N atom, thereby reducing side reactions and enhancing the controllability of the LAPISA process.

Additionally, from the $^1$H NMR spectrum for the crude $PtBMA_{37}$-*b*-$P4VP_{70}$ diblock copolymer (Figure S5), besides the characteristic resonance signal at 1.49 ppm attributed to the protons ($-\text{C}(\text{C}\boldsymbol{H}_3)_3$) on P*t*BMA, the characteristic resonance signals at 6.20–6.70 and 8.00–8.70 ppm attributed to the protons ($-\text{C}_5\boldsymbol{H}_5\text{N}$) on P4VP could also be observed. Especially, the absence of resonance signals from the protons ($\text{C}\boldsymbol{H}_2{=}\text{C}-$) on the double bond of the *t*BMA monomer around 5.46 and 6.00 ppm, as well as the protons ($\text{C}\boldsymbol{H}_2{=}\text{C}\boldsymbol{H}-$) on the double bonds of the 4VP monomer around 6.57, 5.37, and 5.87 ppm, confirmed the complete conversion of *t*BMA and 4VP monomers. Thus, with optimized $[\text{KHMDS}]_0/[\text{DPH}^-\text{Li}^+]_0$ and $[i\text{Bu}_3\text{Al}]_0/[4\text{VP}]_0$ ratios, the LAPISA process in a heterogeneous system could be successfully realized in THF solvent, and P*t*BMA-*b*-P4VP nano-objects could be prepared.

**Factors on Morphological Evolution in the LAPISA Process.** Generally, the solvent has a significant effect on the PISA process. Thus, the effect of the solvent was further investigated by introducing toluene into the toluene/THF solvent. As toluene was a good solvent for P*t*BMA but a poor solvent for P4VP, the introduction of toluene would further decrease the solubility of the P4VP block and induce morphological evolution in the LAPISA process. Meanwhile, the solubility of the P*t*BMA-*b*-P4VP diblock copolymer also depended on the length of the P4VP block. Thus, $M_{n,P4VP}$ was relatively fixed, and the effect of targeted $M_{n,P4VP}/M_{n,PtBMA}$ on morphological evolution was also investigated. As shown in Table 2, a series of formulations were designed and performed to investigate the morphological evolution of nano-objects in


https://doi.org/10.1021/acs.macromol.5c01443
Macromolecules 2025, 58, 8898–8908

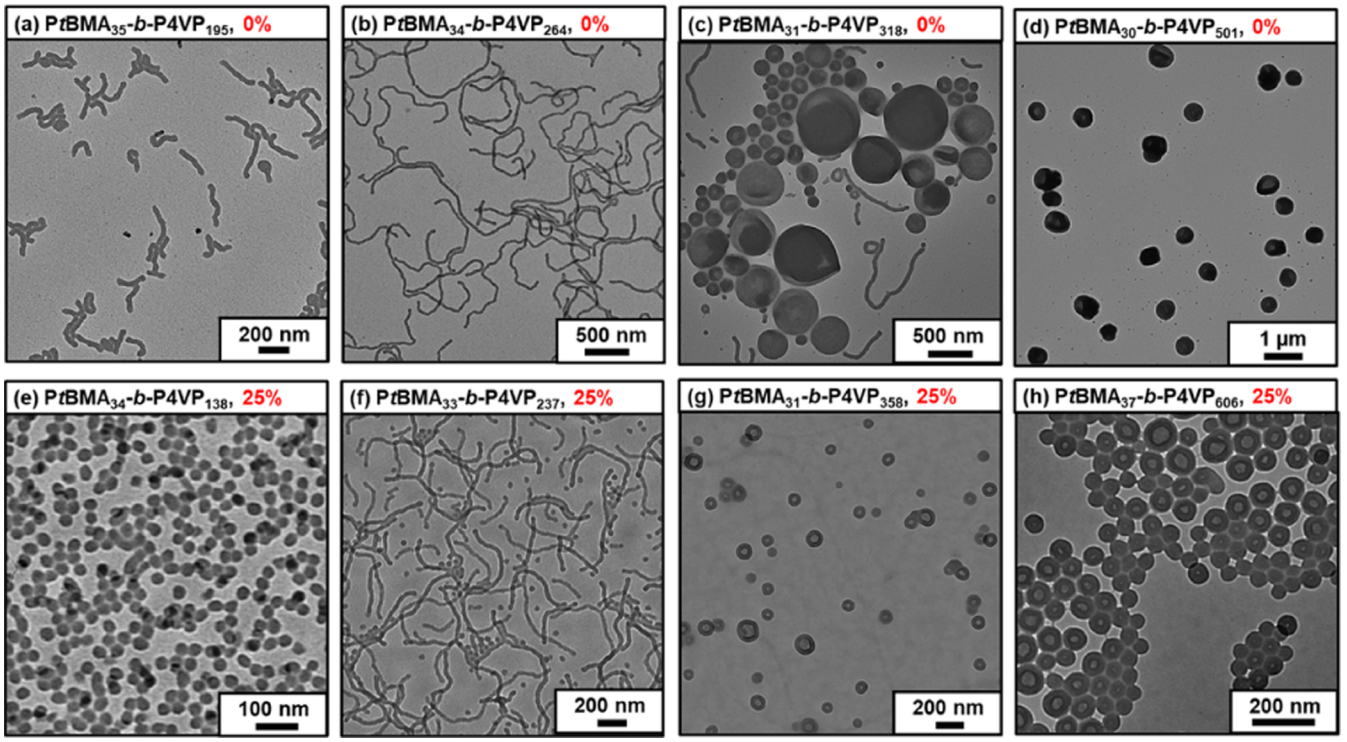


**Figure 3.** TEM images of nano-objects formed by the LAPISA process with $[KHMDS]_0/[DPH^-Li^+]_0$ of 1.0, $[iBu_3Al]_0/[4VP]_0$ of 0.02, solid content of 15 wt %, relatively fixed $M_{n,PtBMA}$ of around 4000−5500, polymerization temperature of 25 °C, different targeted $M_{n,P4VP}/M_{n,PtBMA}$ ratios and wt $\%_{Tol}$ of (a−d) 0% and (e−h) 25% (diluted to 0.1−0.3 wt % dispersions in the corresponding solvent).

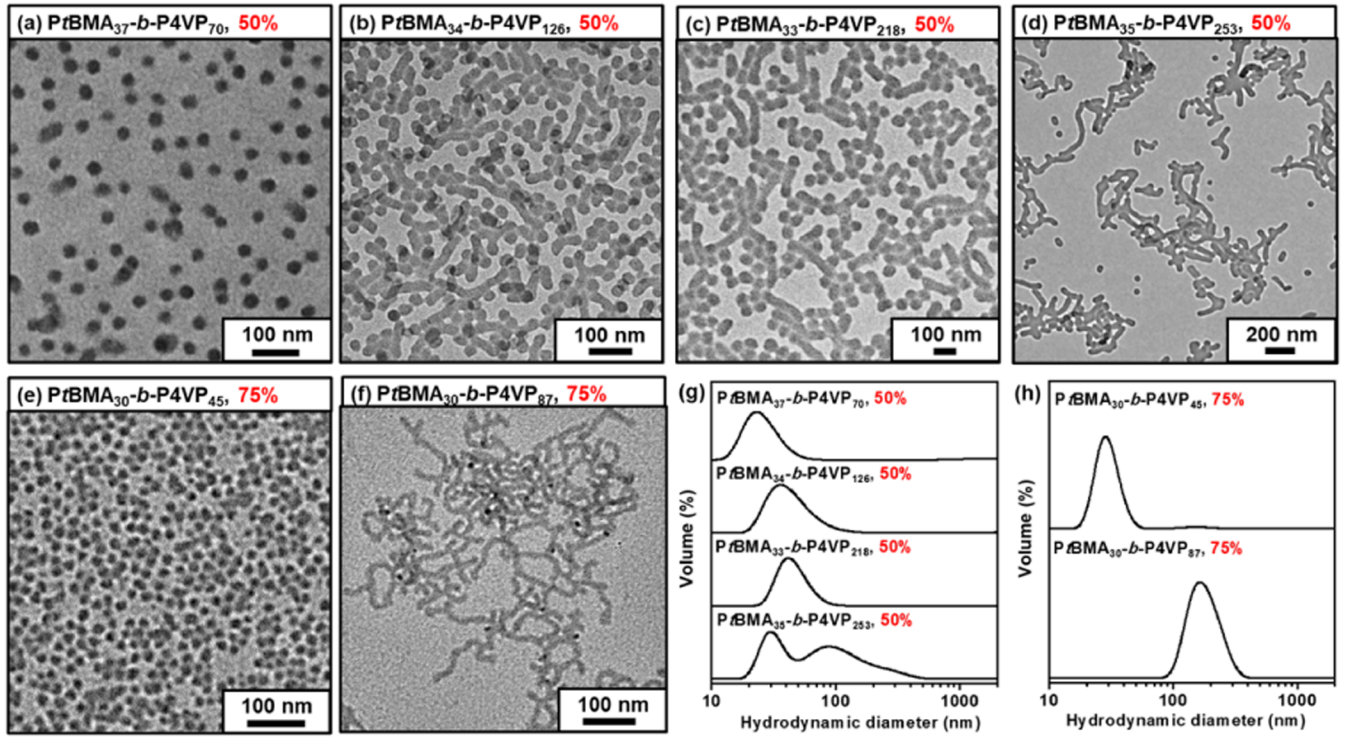


**Figure 4.** TEM images of nano-objects formed by LAPISA process with $[KHMDS]_0/[DPH^-Li^+]_0$ as 1.0, $[iBu_3Al]_0/[4VP]_0$ as 0.02, fixed solid content of 15 wt %, relatively fixed $M_{n,PtBMA}$ around 4000−5500, polymerization temperature of 25 °C, different targeted $M_{n,P4VP}/M_{n,PtBMA}$ and wt $\%_{Tol}$ of 50% (a−d) and 25% (e−f), DLS results of the corresponding nano-objects (g, h) (diluted to 0.1−0.3 wt % dispersions).

the LAPISA process, with the optimized $[KHMDS]_0/[DPH^-Li^+]_0$ as 1.0, $[iBu_3Al]_0/[4VP]_0$ as 0.02, fixed solid content of 15 wt %, relatively fixed $M_{n,PtBMA}$ of around 4000−5500, and a polymerization temperature of 25 °C. The SEC results of the prepared P*t*BMA-*b*-P4VP diblock copolymers



https://doi.org/10.1021/acs.macromol.5c01443
Macromolecules 2025, 58, 8898−8908

and P*t*BMA precursor were shown in Figure S6, and the DLS results were provided in Table 2.

As shown in Table 2 and Figure 3, the cases with pure THF (wt $\%_{Tol}$ of 0%) and varied targeted $M_{n,P4VP}/M_{n,PtBMA}$ ratios were first investigated. For targeted $M_{n,P4VP}/M_{n,PtBMA}$ of 3.0, P*t*BMA$_{34}$-*b*-P4VP$_{107}$ diblock copolymer was generated, and no regular nano-objects could be found in the LAPISA system. The DLS curve in Figure S7 shows a peak at 4 nm, indicating that the P*t*BMA$_{34}$-*b*-P4VP$_{107}$ diblock copolymer did not self-assemble in THF but instead existed as dissolved individual copolymer chains. For targeted $DP_{PtBMA}/DP_{P4VP}$ of 4.0, the P*t*BMA$_{35}$-*b*-P4VP$_{195}$ diblock copolymer was generated, and short worm-like nano-objects could be observed in the TEM image (Figure 3a). For targeted $DP_{PtBMA}/DP_{P4VP}$ of 6.0, the P*t*BMA$_{34}$-*b*-P4VP$_{264}$ diblock copolymer was generated, and long worm-like nano-objects could be observed in the TEM image (Figure 3b). For targeted $M_{n,P4VP}/M_{n,PtBMA}$ of 9.0, the P*t*BMA$_{31}$-*b*-P4VP$_{318}$ diblock copolymer was generated, and a mixture of short worm-like and vesicular nano-objects could be collected (Figure 3c). When the targeted $M_{n,P4VP}/M_{n,PtBMA}$ was increased to 12.0, the vesicular nano-objects with thick walls were observed for the P*t*BMA$_{30}$-*b*-P4VP$_{501}$ diblock copolymer (Figure 3d). Finally, upon further increasing the targeted $M_{n,P4VP}/M_{n,PtBMA}$ to 15.0, P*t*BMA$_{34}$-*b*-P4VP$_{580}$ diblock copolymer was generated, and the precipitate was formed in the LAPISA process. When the wt $\%_{Tol}$ was increased to 25%, the solubility of P4VP was further decreased. For targeted $M_{n,P4VP}/M_{n,PtBMA}$ of 3.0, the P*t*BMA$_{34}$-*b*-P4VP$_{138}$ diblock copolymer was generated, and spherical nano-objects were obtained (Figure 3e). When the targeted $M_{n,P4VP}/M_{n,PtBMA}$ was increased to 6.0, a mixture of spherical and worm-like nano-objects was observed for the P*t*BMA$_{33}$-*b*-P4VP$_{237}$ diblock copolymer (Figure 3f). When the targeted $M_{n,P4VP}/M_{n,PtBMA}$ was increased to 9.0 and 12.0, the vesicular nano-objects were observed from the P*t*BMA$_{31}$-*b*-P4VP$_{358}$ and P*t*BMA$_{37}$-*b*-P4VP$_{606}$ diblock copolymers (Figure 3g,h), respectively.

Furthermore, by increasing the wt $\%_{Tol}$ to 50% and maintaining the targeted $M_{n,P4VP}/M_{n,PtBMA}$ at 1.0 and 2.0, the P*t*BMA$_{34}$-*b*-P4VP$_{49}$ and P*t*BMA$_{37}$-*b*-P4VP$_{70}$ diblock copolymers were generated. The TEM image showed that the spherical nano-objects were formed from P*t*BMA$_{37}$-*b*-P4VP$_{70}$ (Figure 4a), and the DLS curve showed that the hydrodynamic diameters of the spherical nano-objects were around 46 nm (Figure 4g). Maintaining the wt $\%_{Tol}$ at 50% and increasing the targeted $M_{n,P4VP}/M_{n,PtBMA}$ to 3.0 and 4.0, the TEM image showed a mixture of spherical and short-worm nano-objects from P*t*BMA$_{34}$-*b*-P4VP$_{126}$ and P*t*BMA$_{33}$-*b*-P4VP$_{218}$ diblock copolymers (Figure 4b,c). By continuously increasing the targeted $M_{n,P4VP}/M_{n,PtBMA}$ to 6.0, the P*t*BMA$_{35}$-*b*-P4VP$_{253}$ diblock copolymer was generated, and a mixture of spherical and short-worm nano-objects was still observed, except that the amount of short-worm nano-objects was further increased (Figure 4d). Increasing the targeted $M_{n,P4VP}/M_{n,PtBMA}$ to 8.0, the P*t*BMA$_{33}$-*b*-P4VP$_{302}$ diblock copolymer was collected, and the LAPISA system formed precipitates. Increasing the wt $\%_{Tol}$ to 75% and maintaining the targeted $M_{n,P4VP}/M_{n,PtBMA}$ at 1.0, the P*t*BMA$_{30}$-*b*-P4VP$_{45}$ diblock copolymer was generated, and spherical nano-objects with a hydrodynamic diameter of 23 nm were obtained (Figure 4e). Keeping the wt $\%_{Tol}$ at 75%, the LAPISA system formed a gel-like state by increasing the targeted $M_{n,P4VP}/M_{n,PtBMA}$ to 2.0, in which the P*t*BMA$_{30}$-*b*-P4VP$_{87}$ diblock copolymer was generated and a worm-like morphology was observed (Figure 4f). The DLS results showed sizes consistent with those obtained from the TEM images (Figure 4h). Finally, when wt $\%_{Tol}$ was set as 100%, the P*t*BMA$_{37}$-*b*-P4VP$_{50}$ diblock copolymer was generated, and the LAPISA system formed a gel-like consistency even at a targeted $M_{n,P4VP}/M_{n,PtBMA}$ of 1.0. The TEM image shows that a seriously entangled worm-like morphology was formed (Figure S8).

Based on the above morphological evolution of nano-objects under varied wt $\%_{Tol}$ and targeted $M_{n,P4VP}/M_{n,PtBMA}$, a morphological distribution diagram was depicted (Figure 5).

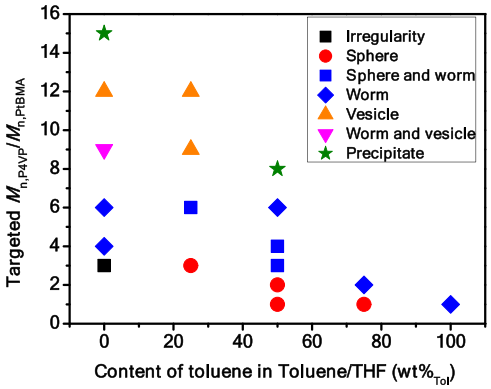


**Figure 5.** Morphological distribution diagram based on the morphologies of nano-objects prepared by the LAPISA process with different targeted $M_{n,P4VP}/M_{n,PtBMA}$ ratios and wt $\%_{Tol}$.

Generally, by decreasing the wt $\%_{Tol}$ and increasing the targeted $M_{n,P4VP}/M_{n,PtBMA}$, the morphologies tended to evolve into a higher-order region. Conversely, with increasing wt $\%_{Tol}$ and decreasing targeted $M_{n,P4VP}/M_{n,PtBMA}$, lower-order spherical morphologies were favored. Without exception, the LAPISA process in our work for polar monomers also obeyed the general principle of a PISA process, in which nano-objects were formed under a thermodynamic equilibrium state. Typically, the morphological evolution of the nano-objects in the PISA process is dominantly affected by the inherent packing of copolymer chains as defined by the packing parameter $P = v/a_0l_c$, where $v$, $a_0$, and $l_c$ represent the volume of the core-forming block, the interfacial area, and the length of the core-forming block, respectively.[54−56] Following this rule, spherical ($P \leq 1/3$), worm-like ($1/3 < P \leq 1/2$), and vesicular ($1/2 < P \leq 1$) micelles can be regularly generated by modulating the $P$ value-related parameters. Correspondingly, in our work, the major parameters affecting the $P$ value were wt $\%_{Tol}$ and $M_{n,P4VP}/M_{n,PtBMA}$. This was because THF and toluene are both good solvents for the P*t*BMA block. However, compared to THF, toluene is a relatively poor solvent for the P4VP block. The solubility of the P4VP block could be modulated by varying wt $\%_{Tol}$. Meanwhile, by varying $M_{n,P4VP}/M_{n,PtBMA}$, the relative volume ratio of the solvophobic P4VP and solvophilic P*t*BMA blocks could also be modulated. Intrinsically, wt $\%_{Tol}$ and $M_{n,P4VP}/M_{n,PtBMA}$ could alter the volume of the core-forming block, the interfacial area, and the length of the core-forming block, which directly affected the $P$ value. Thus, nano-objects with different morphologies could be modulated and their potential applications could be guided.

**Stabilization and Functionalization of the Nano-Objects Formed in LAPISA Process.** After the LAPISA process, the pyridine groups in the core region could be crosslinked by a quaternization reaction with 1,4-dibromobu-


https://doi.org/10.1021/acs.macromol.5c01443
Macromolecules 2025, 58, 8898−8908

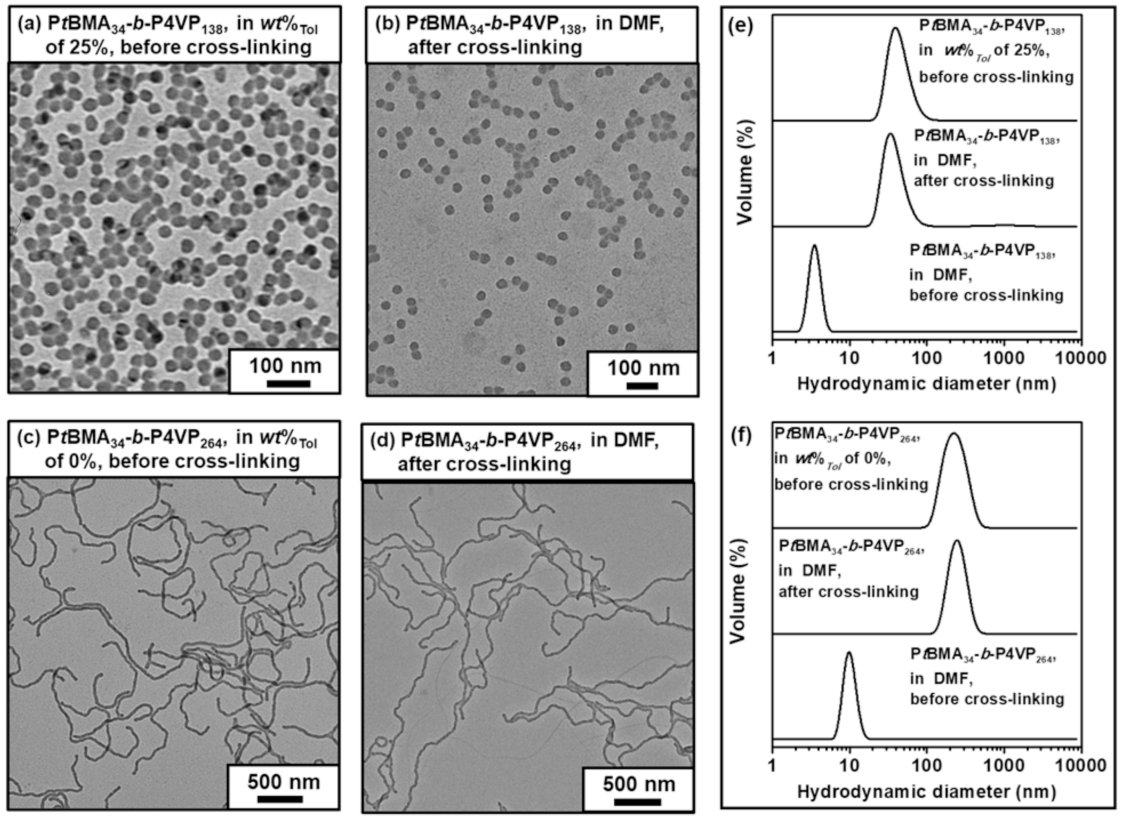


**Figure 6.** TEM images of unstabilized nano-objects in the original solvent for the LAPISA process (a, c) and stabilized nano-objects in DMF (b, d) (diluted to 0.1−0.3 wt % dispersions). DLS curves for the corresponding stabilized and unstabilized nano-objects (e, f).

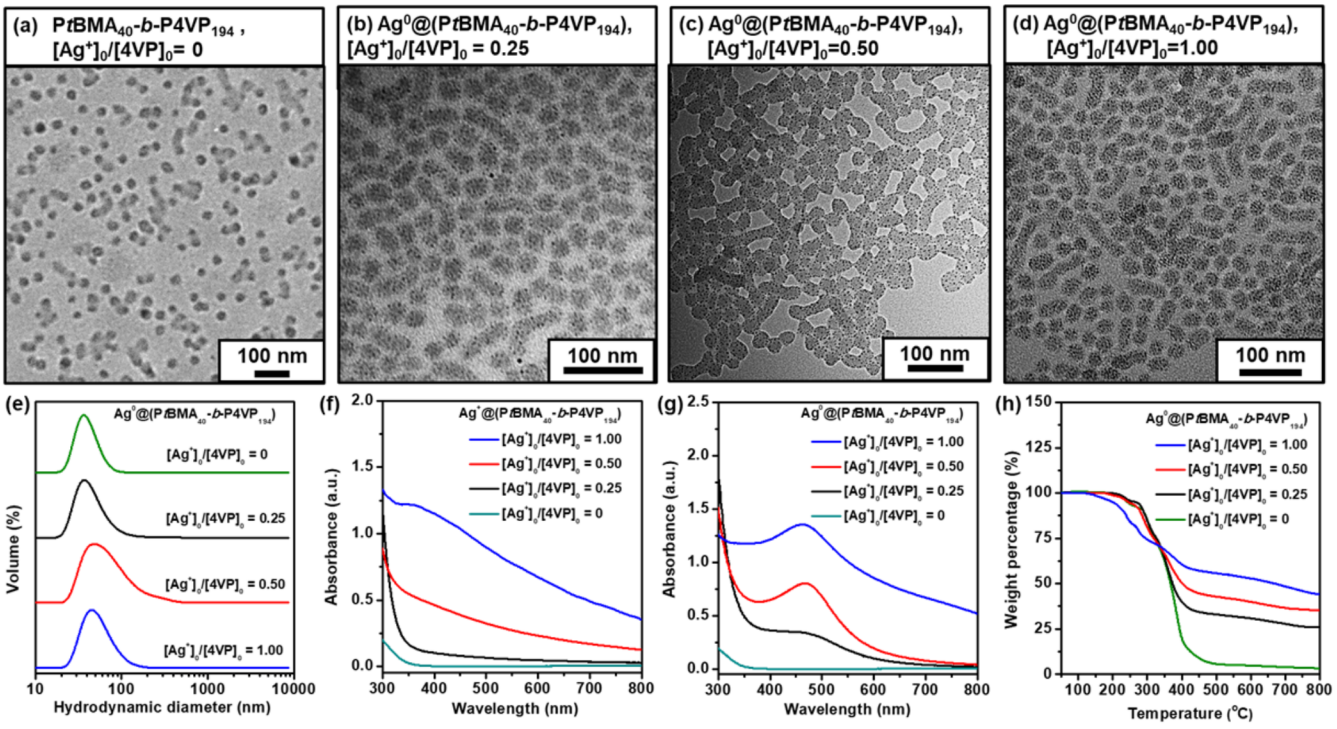


**Figure 7.** TEM images of $Ag^0$@($PtBMA_{40}$-*b*-$P4VP_{194}$) nano-objects incorporated with different amounts of $Ag^0$ (a−d) (diluted to 0.1−0.3 wt % dispersions in THF). (e) DLS curves of the corresponding $Ag^0$@($PtBMA_{40}$-*b*-$P4VP_{194}$) nano-objects (diluted to 0.1−0.3 wt % dispersions in DMF). (f, g) UV−vis spectra of $Ag^+$@($PtBMA_{40}$-*b*-$P4VP_{194}$) and $Ag^0$@($PtBMA_{40}$-*b*-$P4VP_{194}$) in DMF. (h) TGA curves of the corresponding $Ag^0$@($PtBMA_{40}$-*b*-$P4VP_{194}$) nano-objects.



https://doi.org/10.1021/acs.macromol.5c01443
*Macromolecules* 2025, 58, 8898−8908

tane. The stabilization of nano-objects with spherical (38 nm, P*t*BMA$_{34}$-*b*-P4VP$_{138}$) and worm-like (255 nm, P*t*BMA$_{34}$-*b*-P4VP$_{246}$) morphologies was used as example. As shown in Figure 6a−d, the stabilized nano-objects in DMF had the same morphologies as the unstabilized ones in THF or toluene/THF from the original LAPISA system. The DLS results also confirmed that the stabilized and unstabilized nano-objects had similar sizes in DMF and THF or toluene/THF, respectively (Figure 6e,f). For a comparison, the size of the unstabilized nano-objects in DMF was measured as 5 nm, as DMF was a simultaneously good solvent for P*t*BMA and P4VP blocks, and the diblock copolymer was sufficiently solubilized. Thus, the good maintenance of the morphologies in DMF solvent provided solid evidence for the successful stabilization of nano-objects. The stabilized nano-objects facilitated further application as the morphologies could remain unchanged under practical conditions, such as in good solvents or under shear forces.

Furthermore, following the diagram in Figure 5, spherical P*t*BMA$_{37}$-*b*-P4VP$_{70}$ nano-objects were prepared, stabilized, and employed as templates for organic/inorganic nanocomposites. That was, $Ag^0$ was introduced into the nano-objects by the first incorporation of pyridine groups on P4VP with $Ag^+$ ions and further reduction reaction with sodium borohydride ($NaBH_4$). As shown in Figure 7a−d, $Ag^0$ in the final $Ag^0$@(P*t*BMA$_{40}$-*b*-P4VP$_{194}$) nano-objects could be clearly distinguished, and the amount of $Ag^0$ could be modulated by changing the feed ratio of $[Ag^+]_0/[4VP]_0$. In all cases, the sizes from the DLS measurements were less different, which confirmed that the incorporation of $Ag^0$ had no obvious effect on the morphologies of the nano-objects (Figure 7e). The UV−vis spectra for $Ag^+$@(P*t*BMA$_{40}$-*b*-P4VP$_{194}$) and $Ag^0$@(P*t*BMA$_{40}$-*b*-P4VP$_{194}$) confirmed that $Ag^+$ and $Ag^0$ were actually introduced. Before the reduction of $Ag^+$, a weak shoulder was observed at 400 nm, which was attributed to the adsorption of $Ag^+$ ions (Figure 7f). After the reduction of $Ag^+$ to $Ag^0$, a peak at 475 nm, attributed to the adsorption of $Ag^0$, was clearly observed (Figure 7g). The UV−vis spectra of $Ag^+$ and $Ag^0$ on $Ag^+$@(P*t*BMA$_{40}$-*b*-P4VP$_{194}$) and $Ag^0$@(P*t*BMA$_{40}$-*b*-P4VP$_{194}$) nano-objects were consistent with the results reported in the literature.[57−59] Especially, with the regular increase of $[Ag^+]_0/[4VP]_0$, the shoulder at 400 nm and peak at 475 nm showed a progressive increase in intensity, respectively. Additionally, the TGA measurement showed that the higher the $Ag^0$ content, the lower the weight loss percentage (Figure 7h). In detail, the weight loss percentage of the P*t*BMA$_{40}$-*b*-P4VP$_{194}$ diblock copolymer was 97%. The $Ag^0$ contents in $Ag^0$@(P*t*BMA$_{40}$-*b*-P4VP$_{194}$) nano-objects with $[Ag^+]_0/[4VP]_0$ ratios of 0.25, 0.50, and 1.00 were measured to be 74% (theoretical 74%), 65% (theoretical 61%), and 56% (theoretical 44%), respectively. Obviously, the measured $Ag^0$ contents were close to or slightly lower than the theoretical values. All these results confirmed that $Ag^0$ was efficiently introduced into the nano-objects in a controlled manner. The well-maintained spherical morphologies after the introduction of $Ag^0$ further confirmed the successful stabilization described in the previous section. Conversely, in the case without stabilization, the added $AgNO_3$ or $NaBH_4$, as well as the shear force by long-time stirring or a good solvent of DMF, might induce the dissociation or re-self-assembly of the already formed nano-objects. The morphology or size of the original nano-objects would be changed and, thus, the function of the LAPISA process would be meaningless.

## CONCLUSIONS

In summary, using polar *t*BA and 4VP monomers, functional P*t*BMA-*b*-P4VP diblock copolymers and nano-objects were successfully prepared by the LAPISA process. To realize smooth polymerization, KHMDS/DPH$^-$Li$^+$ was used as a co-initiation system, and *i*Bu$_3$Al was used as an additive. To modulate the morphologies of the nano-objects, $[KHMDS]_0/[DPH^-Li^+]_0$, $[iBu_3Al]_0/[4VP]_0$, targeted $M_{n,P4VP}/M_{n,PtBMA}$, and wt $\%_{Tol}$ were systematically investigated, and a library of spherical, worm-like, and vesicular nano-objects was prepared. To stabilize the nano-objects, the P4VP core was crosslinked via a quaternization reaction between pyridine groups and 1,4-dibromobutane. To functionalize the nano-objects, $Ag^0$ was introduced by complexation with $Ag^+$ and a reduction reaction, and the $Ag^0$ content was well modulated. Unlike the traditional LAP of polar vinyl monomers (such as methyl methacrylate (MMA), 2-vinylpyridine (2VP), 4VP, etc., at −78 °C[60−64]), the LAPISA process in this work eliminated the need for low-temperature operation while maintaining good control in a heterogeneous system at room temperature. Meanwhile, the functional nano-objects could serve as templates for the preparation of organic/inorganic nanocomposites.

## ASSOCIATED CONTENT

### Supporting Information

The Supporting Information is available free of charge at https://pubs.acs.org/doi/10.1021/acs.macromol.5c01443.

Experimental procedures for the synthesis and additional characterization data, including Figures S1−S8 and Table S1 (PDF)

## AUTHOR INFORMATION


### Corresponding Author

**Guowei Wang** − *State Key Laboratory of Molecular Engineering of Polymers, Department of Macromolecular Science, Fudan University, Shanghai 200433, China;* orcid.org/0000-0003-2595-8269; Email: gwwang@fudan.edu.cn

### Author

**Di Li** − *State Key Laboratory of Molecular Engineering of Polymers, Department of Macromolecular Science, Fudan University, Shanghai 200433, China;* orcid.org/0000-0001-9017-9582

Complete contact information is available at: https://pubs.acs.org/10.1021/acs.macromol.5c01443


### Notes

The authors declare no competing financial interest.

## ACKNOWLEDGMENTS

*This work is supported by the National Natural Science Foundation of China (22271058).

## REFERENCES


(1) Discher, B. M.; Won, Y. Y.; Ege, D. S.; et al. Polymersomes: tough vesicles made from diblock copolymers. *Science* **1999**, *284* (5417), 1143−1146.

(2) Zhang, L.; Eisenberg, A. Multiple morphologies of″ crew-cut″ aggregates of polystyrene-*b*-poly (acrylic acid) block copolymers. *Science* **1995**, *268* (5218), 1728−1731.

(3) Zhang, L.; Eisenberg, A. Thermodynamic vs kinetic aspects in the formation and morphological transitions of crew-cut aggregates produced by self-assembly of polystyrene-*b*-poly (acrylic acid) block copolymers in dilute solution. *Macromolecules* **1999**, *32* (7), 2239−2249.
(4) Zhang, L.; Eisenberg, A. Multiple morphologies and characteristics of "crew-cut" micelle-like aggregates of polystyrene-*b*-poly (acrylic acid) diblock copolymers in aqueous solutions. *J. Am. Chem. Soc.* **1996**, *118* (13), 3168−3181.
(5) Shen, H.; Eisenberg, A. Block length dependence of morphological phase diagrams of the ternary system of PS-*b*-PAA/dioxane/$H_2O$. *Macromolecules* **2000**, *33* (7), 2561−2572.
(6) Shi, B.; Zhang, H.; Liu, Y.; et al. Development of ICAR ATRP−Based Polymerization-Induced Self-Assembly and Its Application in the Preparation of Organic−Inorganic Nanoparticles. *Macromol. Rapid Commun.* **2019**, *40* (24), No. 1900547.
(7) Douverne, M.; Ning, Y.; Tatani, A.; et al. How many phosphoric acid units are required to ensure uniform occlusion of sterically stabilized nanoparticles within calcite? *Angew. Chem., Int. Ed.* **2019**, *131* (26), 8784−8789.
(8) Ning, Y.; Han, L.; Douverne, M.; et al. What dictates the spatial distribution of nanoparticles within calcite? *J. Am. Chem. Soc.* **2019**, *141* (6), 2481−2489.
(9) Ding, Z.; Ding, M.; Gao, C.; et al. In Situ Synthesis of Coil−Coil Diblock Copolymer Nanotubes and Tubular Ag/Polymer Nanocomposites by RAFT Dispersion Polymerization in Poly (Ethylene Glycol). *Macromolecules* **2017**, *50* (19), 7593−7602.
(10) Zhang, X.; Cardozo, A. F.; Chen, S.; et al. Core−shell nanoreactors for efficient aqueous biphasic catalysis. *Chem. - Eur. J.* **2014**, *20* (47), 15505−15517.
(11) Hinderling, C.; Keles, Y.; Stöckli, T.; et al. Organometallic block copolymers as catalyst precursors for templated carbon nanotube growth. *Adv. Mater.* **2004**, *16* (11), 876−879.
(12) Han, H.; Oh, J. W.; Park, J.; et al. Hierarchically Ordered Perovskites with High Photo-Electronic and Environmental Stability via Nanoimprinting Guided Block Copolymer Self-Assembly. *Adv. Mater. Interfaces* **2022**, *9* (16), No. 2200082.
(13) Huang, J.; Liu, D.; Chen, Y.; et al. Preparation of Block Copolymer Nano-Objects with Embedded *β*-Ketoester Functional Groups by Photoinitiated RAFT Dispersion Polymerization. *Macromol. Rapid Commun.* **2021**, *42* (7), No. 2000720.
(14) Huo, M.; Ye, Q.; Che, H.; et al. Polymer assemblies with nanostructure-correlated aggregation-induced emission. *Macromolecules* **2017**, *50* (3), 1126−1133.
(15) Rösler, A.; Vandermeulen, G. W.; Klok, H.-A. Advanced drug delivery devices via self-assembly of amphiphilic block copolymers. *Adv. Drug Delivery Rev.* **2012**, *64*, 270−279.
(16) Thambi, T.; Son, S.; Lee, D. S.; Park, J. H. Poly (ethylene glycol)-*b*-poly (lysine) copolymer bearing nitroaromatics for hypoxia-sensitive drug delivery. *Acta Biomater.* **2016**, *29*, 261−270.
(17) Cordella, D.; Ouhib, F.; Aqil, A.; et al. Fluorinated poly (ionic liquid) diblock copolymers obtained by cobalt-mediated radical polymerization-induced self-assembly. *ACS Macro Lett.* **2017**, *6* (2), 121−126.
(18) Demarteau, J.; de Añastro, A. F.; Shaplov, A. S.; Mecerreyes, D. Poly (diallyldimethylammonium) based poly (ionic liquid) di-and triblock copolymers by PISA as matrices for ionogel membranes. *Polym. Chem.* **2020**, *11* (8), 1481−1488.
(19) Chung, T. C.; Janvikul, W.; Bernard, R.; Jiang, G. J. Synthesis of ethylene-propylene rubber graft copolymers by borane approach. *Macromolecules* **1994**, *27* (1), 26−31.
(20) Arotçaréna, M.; Heise, B.; Ishaya, S.; Laschewsky, A. Switching the inside and the outside of aggregates of water-soluble block copolymers with double thermoresponsivity. *J. Am. Chem. Soc.* **2002**, *124* (14), 3787−3793.
(21) Thurmond, K. B.; Kowalewski, T.; Wooley, K. L. Water-soluble knedel-like structures: the preparation of shell-cross-linked small particles. *J. Am. Chem. Soc.* **1996**, *118* (30), 7239−7240.
(22) Shen, H.; Zhang, L.; Eisenberg, A. Thermodynamics of crew-cut micelle formation of polystyrene-*b*-poly (acrylic acid) diblock copolymers in DMF/H2O mixtures. *J. Phys. Chem. B* **1997**, *101* (24), 4697−4708.
(23) Yu, K.; Eisenberg, A. Bilayer morphologies of self-assembled crew-cut aggregates of amphiphilic PS-*b*-PEO diblock copolymers in solution. *Macromolecules* **1998**, *31* (11), 3509−3518.
(24) Derry, M. J.; Fielding, L. A.; Armes, S. P. Industrially-relevant polymerization-induced self-assembly formulations in non-polar solvents: RAFT dispersion polymerization of benzyl methacrylate. *Polym. Chem.* **2015**, *6* (16), 3054−3062.
(25) Cunningham, V. J.; Alswieleh, A. M.; Thompson, K. L.; et al. Poly (glycerol monomethacrylate)−poly (benzyl methacrylate) diblock copolymer nanoparticles via RAFT emulsion polymerization: synthesis, characterization, and interfacial activity. *Macromolecules* **2014**, *47* (16), 5613−5623.
(26) Wang, J.; Wu, Z.; Wang, G.; Matyjaszewski, K. In Situ Crosslinking of Nanoparticles in Polymerization-Induced Self-Assembly via ARGET ATRP of Glycidyl Methacrylate. *Macromol. Rapid Commun.* **2019**, *40* (2), No. 1800332.
(27) Wang, G.; Schmitt, M.; Wang, Z.; et al. Polymerization-induced self-assembly (PISA) using ICAR ATRP at low catalyst concentration. *Macromolecules* **2016**, *49* (22), 8605−8615.
(28) Wan, W.-M.; Pan, C.-Y. Atom transfer radical dispersion polymerization in an ethanol/water mixture. *Macromolecules* **2007**, *40* (25), 8897−8905.
(29) Sugihara, S.; Armes, S. P.; Lewis, A. L. One-pot synthesis of biomimetic shell cross-linked micelles and nanocages by ATRP in alcohol/water mixtures. *Angew. Chem., Int. Ed.* **2010**, *49* (20), 3500−3503.
(30) Derry, M. J.; Mykhaylyk, O. O.; Armes, S. P. A vesicle-to-worm transition provides a new high-temperature oil thickening mechanism. *Angew. Chem., Int. Ed.* **2017**, *129* (7), 1772−1776.
(31) György, C.; Armes, S. P. Recent Advances in Polymerization-Induced Self-Assembly (PISA) Syntheses in Non-Polar Media. *Angew. Chem., Int. Ed.* **2023**, No. e202308372.
(32) Delaittre, G.; Dire, C.; Rieger, J.; et al. Formation of polymer vesicles by simultaneous chain growth and self-assembly of amphiphilic block copolymers. *Chem. Commun.* **2009**, No. 20, 2887−2889.
(33) Groison, E.; Brusseau, S.; D'Agosto, F.; et al. Well-defined amphiphilic block copolymer nanoobjects via nitroxide-mediated emulsion polymerization. *ACS Macro Lett.* **2012**, *1* (1), 47−51.
(34) Ulker, D.; Neal, T. J.; Crawford, A.; Armes, S. P. Thermoresponsive Poly (N, N′-dimethylacrylamide)-Based Diblock Copolymer Worm Gels via RAFT Solution Polymerization: Synthesis, Characterization, and Cell Biology Applications. *Biomacromolecules* **2023**, *24* (9), 4285−4302.
(35) Zhou, J.; Huang, Q.; Zhang, L.; Tan, J. Exploiting the Monomer-Feeding Mechanism of RAFT Emulsion Polymerization for Polymerization-Induced Self-Assembly of Asymmetric Divinyl Monomers. *ACS Macro Lett.* **2023**, *12*, 1457−1465.
(36) Zhang, Y.; Yu, L.; Dai, X.; et al. Structural difference in macro-RAFT agents redirects polymerization-induced self-assembly. *ACS Macro Lett.* **2019**, *8* (9), 1102−1109.
(37) Tan, J.; Huang, C.; Liu, D.; et al. Polymerization-induced self-assembly of homopolymer and diblock copolymer: A facile approach for preparing polymer nano-objects with higher-order morphologies. *ACS Macro Lett.* **2017**, *6* (3), 298−303.
(38) Neal, T. J.; Penfold, N. J.; Armes, S. P. Reverse Sequence Polymerization-Induced Self-Assembly in Aqueous Media. *Angew. Chem., Int. Ed.* **2022**, *134* (33), No. e202207376.
(39) Kitayama, Y.; Chaiyasat, A.; Okubo, M. Emulsifier-Free, Organotellurium-Mediated Living Radical Emulsion Polymerization of Styrene. In *Macromol. Symp.*; Wiley Online Library, 2010; Vol. *288*, pp 25−32.
(40) Zhou, D.; Kuchel, R. P.; Zetterlund, P. B. A new paradigm in polymerization induced self-assembly (PISA): Exploitation of "non-


https://doi.org/10.1021/acs.macromol.5c01443
*Macromolecules* 2025, 58, 8898−8908

living" addition−fragmentation chain transfer (AFCT) polymerization. *Polym. Chem.* **2017**, *8* (29), 4177−4181.
(41) Zhang, L.; Song, C.; Yu, J.; et al. One-pot synthesis of polymeric nanoparticle by ring-opening metathesis polymerization. *J. Polym. Sci., Part A: Polym. Chem.* **2010**, *48* (22), 5231−5238.
(42) Le, D.; Dilger, M.; Pertici, V.; et al. Ultra-Fast Synthesis of Multivalent Radical Nanoparticles by Ring-Opening Metathesis Polymerization-Induced Self-Assembly. *Angew. Chem., Int. Ed.* **2019**, *58* (14), 4725−4731.
(43) Tanaka, S.; Matsumoto, M.; Goseki, R.; et al. Living anionic polymerization of 1, 4-divinylbenzene and its isomers. *Macromolecules* **2013**, *46* (1), 146−154.
(44) Baskaran, D. Strategic developments in living anionic polymerization of alkyl (meth) acrylates. *Prog. Polym. Sci.* **2003**, *28* (4), 521−581.
(45) Takenaka, K.; Hirao, A.; Hattori, T.; Nakahama, S. Polymerization of monomers containing functional silyl groups. 4. Anionic polymerization of 2-(trimethoxysilyl)-1, 3-butadiene. *Macromolecules* **1987**, *20* (8), 2034−2035.
(46) Yang, L.; Ma, H.; Han, L.; et al. Sequence features of sequence-controlled polymers synthesized by 1, 1-diphenylethylene derivatives with similar reactivity during living anionic polymerization. *Macromolecules* **2018**, *51* (15), 5891−5903.
(47) Wang, X.; Hall, J. E.; Warren, S.; et al. Synthesis, characterization, and application of novel polymeric nanoparticles. *Macromolecules* **2007**, *40* (3), 499−508.
(48) Wang, J.; Cao, M.; Zhou, P.; Wang, G. Exploration of a living anionic polymerization mechanism into polymerization-induced self-assembly and site-specific stabilization of the formed nano-objects. *Macromolecules* **2020**, *53* (8), 3157−3165.
(49) Zhou, C.; Wang, J.; Zhou, P.; Wang, G. A polymerization-induced self-assembly process for all-styrenic nano-objects using the living anionic polymerization mechanism. *Polym. Chem.* **2020**, *11* (15), 2635−2639.
(50) Zhang, J.; Zhou, P.; Shi, B.; et al. High-Efficient Access to Inverse Morphologies via Living Anionic Polymerization-Mediated Polymerization-Induced Cooperative Assembly. *Macromolecules* **2023**, *56* (15), 5743−5753.
(51) Kitaura, T.; Kitayama, T. Anionic polymerization of methyl methacrylate by difunctional lithium amide initiators with trialkylsilyl protection. *Polym. J.* **2013**, *45* (10), 1013−1018.
(52) Creutz, S.; Teyssié, P.; Jérôme, R. Anionic block copolymerization of 4-vinylpyridine and tert-butyl methacrylate at "elevated" temperatures: influence of various additives on the molecular parameters. *Macromolecules* **1997**, *30* (19), 5596−5601.
(53) Pasynkiewicz, S.; Diem, T. Polymerization of complexes formed by 4-vinylpyridine with alkylaluminium compounds and aluminium chloride. *Macromol. Chem. Phys.* **1970**, *136* (1), 137−146.
(54) Canning, S. L.; Smith, G. N.; Armes, S. P. A Critical Appraisal of RAFT-Mediated Polymerization-Induced Self Assembly. *Macromolecules* **2016**, *49* (6), 1985−2001.
(55) Derry, M. J.; Fielding, L. A.; Armes, S. P. Polymerization-induced self-assembly of block copolymer nanoparticles via RAFT non-aqueous dispersion polymerization. *Prog. Polym. Sci.* **2016**, *52*, 1−18.
(56) György, C.; Armes, S. P. Recent Advances in Polymerization-Induced Self-Assembly (PISA) Syntheses in Non-Polar Media. *Angew. Chem., Int. Ed.* **2023**, *62* (42), No. e202308372.
(57) Lu, H. W.; Liu, S. H.; Wang, X. L.; Qian, X. F.; Yin, J.; Zhu, Z. K. Silver nanocrystals by hyperbranched polyurethane-assisted photochemical reduction of $Ag^{+}$. *Mater. Chem. Phys.* **2003**, *81* (1), 104−107.
(58) Kozioł, R.; Lapinski, M.; Syty, P.; Koszelow, D.; Sadowski, W.; Sienkiewicz, J. E.; Koscielska, B. Evolution of Ag nanostructures created from thin films: UV−vis absorption and its theoretical predictions. *Beilstein J. Nanotechnol.* **2020**, *11*, 494−507.
(59) Ikram, M.; Akhtar, T.; Shujah, T.; Haider, A.; Shahzadi, I.; Haider, A. M.; Ul-Hamid, A.; Fouda, A. M. Bifunctional properties of silver and polyvinylpyrrolidone modified multi-phase MnO2 for enhanced RhB degradation and DNA gyrase/DHFR targeted bactericidal potential. *Mater. Chem. Phys.* **2025**, *345*, No. 131254.
(60) Baskaran, D. Strategic developments in living anionic polymerization of alkyl (meth)acrylates. *Prog. Polym. Sci.* **2003**, *28* (4), 521−581.
(61) Vlček, P.; Lochmann, L. Anionic polymerization of (meth)-acrylate esters in the presence of stabilizers of active centres. *Prog. Polym. Sci.* **1999**, *24* (6), 793−873.
(62) Kuo, S.-W.; Tung, P.-H.; Chang, F.-C. Syntheses and the study of strongly hydrogen-bonded poly(vinylphenol-*b*-vinylpyridine) diblock copolymer through anionic polymerization. *Macromolecules* **2006**, *39* (26), 9388−9395.
(63) Tsitsilianis, C.; Voyiatzis, G. A.; Kallitsis, J. K. Synthesis of coil-rod-coil block copolymers with the aid of anionic polymerization. *Macromol. Rapid Commun.* **2000**, *21* (16), 1130−1135.
(64) Zheng, K.; He, J.-P. Amphiphilic Dendrimer-like Copolymers with High Chain Density by Living Anionic Polymerization. *Chin. J. Polym. Sci.* **2019**, *37* (9), 875−883.




https://doi.org/10.1021/acs.macromol.5c01443
*Macromolecules* 2025, 58, 8898−8908